Boron-doped rutile TiO_2/ anatase TiO_2/ $ZrTiO_4$ ternary heterojunction photocatalyst with optimized phase interface and band structure

Changqing Liu[a,], Xu Li[a], Chenggang Xu[a], Yuanting Wu[a], Xuefeng Hu[b], Xianghui Hou[c,*]*

[a]School of Material Science and Engineering, Shaanxi Key Laboratory of Green Preparation and Functionalization for Inorganic Materials, Shaanxi University of Science & Technology, Xi'an 710021, PR China

[b]School of Environmental Science and Engineering, Shaanxi University of Science & Technology, Xi'an 710021, PR China

[c]Advanced Materials Research Group, Faculty of Engineering, The University of Nottingham, Nottingham, NG7 2RD, UK

Abstract

To improve the photocatalytic performance of TiO_2-based heterostructures, Z-scheme/Ⅱ-type rutile TiO_2 (R) / anatase TiO_2 (A) / $ZrTiO_4$ ternary heterojunction photocatalyst was designed and prepared via a facile one-step calcining strategy. Phase interface and band structure of the materials were controlled and optimized by regulating R-TiO_2 /A-TiO_2 mass ratio in the TiO_2 (A, R)/ $ZrTiO_4$ structures using boron doping. The highest photocatalytic performance and excellent catalytic stability of Rhodamine B removal was observed from the heterojunction with a low R-TiO_2

*Corresponding author. Tel.: +86 15129053527. E-mail address: liu280097311@163.com (C.Q. Liu).

/A-TiO_2 mass ratio of 0.066, even after five testing cycles, accompanying with low photoluminescence intensity and electrochemical impedance, high photocurrent and charge carrier density (5.12×10^{22} cm^{-3}), and a positive shift of valence band position (from + 2.06 to + 2.16 eV). The increased photodegradation behaviour was due to the remarkably enhanced separation efficiency and improved redox ability of the photo-induced charge carriers as a result of the high content of oxygen vacancies and the formed anatase TiO_2 /rutile TiO_2 Z-scheme heterojunction.

Keywords: B: Interface; B: Surface; D: Rutile TiO_2 / Anatase TiO_2 / $ZrTiO_4$; E: Functional application

1. Introduction

The increasing energy and environmental crises are challenging the global social and economic development. Semiconductor-based photocatalytic technique with the advantages of high efficiency, low cost, clean, renewable, and universality has been extensively researched and used in wastewater remediation and energy conversion [1-7]. Because of the unique physical and photochemical properties, TiO_2 has become the most widely studied photocatalytic material among numerous metal oxides semiconductors. However, the narrow absorption of solar spectrum, slow separation of photo-induced charge carriers, and low efficiency of interfacial charge transfer are still limiting its further application [8-10].

To overcome the above issues of TiO_2, phase junction optimization through semiconductor coupling has been demonstrated to be an effective approach. To date, TiO_2 coupled with binary semiconductor, such as TiO_2/ZnO, TiO_2/CuO, TiO_2/ZrO_2, TiO_2/MgO have been successfully synthesized and applied in the area of organic pollutants degradation and hydrogen production [11-15]. Besides, a novel ternary oxide semiconductor, zirconium titanate ($ZrTiO_4$), has attracted more and more attention due to the similar crystal structure, matched band gap energies, high negative conduction band potential, and high chemical stability, as compared with TiO_2. The characteristic of $ZrTiO_4$ shows great potential to form well-structured TiO_2/$ZrTiO_4$ heterojunction, which has verified the effectiveness on the separation of photo-induced electron-hole pairs, and the improvement on photocatalytic activities [16].

Whereas, for conventional heterojunction photocatalysts, the redox ability of photo-induced charge carriers is weakened for separated and transferred charges at the interface [17]. The photo-induced electrons and holes with the strong redox ability can be retained to participate in photocatalytic reactions by constructing Z-scheme heterojunctions [18]. However, Z-scheme photocatalytic materials are usually prepared with the aid of the electron mediators, including noble metals (Pd, Pt, Au, Ag), carbon-based materials (CQDs, GQDs, RGO) or redox pairs (IO^{3-}/I^{-}, Fe^{3+}/Fe^{2+}, NO^{3-}/NO^{2-}), resulting in limited practical applications due to the high-cost and complex operation [19,20]. Therefore, a new concept on the Z-type TiO_2 based photocatalytic systems need to be explored.

Element doping is a feasible approach to tune the intrinsic electronic band structures and optical properties for highly active photocatalysts [21-24]. Currently, the element doping can be summarized into two categories: metal element (Al, Zn, et al) doping, and non-metal element (B, C, N, O, S, et al) doping. Unfortunately, due to the inevitable defects of metal element doping, such as low thermal stability, increased recombination centres of photocatalytic electron-hole (e^{-}-h^{+}) pairs and possible secondary pollution caused by photo-corrosion, metal element doping is not an ideal method to choose [25,26]. Contrarily, the non-metal element doping has been extensively applied owing to their high thermal stability and the ability to modulate electronic properties of the materials [27,28]. Among these non-metal elements, boron doping has already been proved to tailor the optical behaviors of TiO_2 based materials by enhancing the electron-accepting capacity of TiO_2. Furthermore, the addition of

boron source (such as H_3BO_3) was an established approach to tune the phase ratio between anatase and rutile TiO_2 [29]. Xu et al. prepared anatase/rutile bi-phase TiO_2 nanofibers composites and proposed that the Z-scheme photocatalytic mechanism was the reason for the improved photocatalytic H_2-production ability [30]. The result suggested that A-TiO_2/R-TiO_2 Z-scheme photocatalysts can be directly obtained by controlling the component of TiO_2 (A, R) as a result of boron doping. Furthermore, to achieve high photocatalytic activity of R-TiO_2/A-TiO_2 Z-scheme photocatalyst, the contact interface between the two phases which mainly determined by the phase ratio must be well controlled to improve charge-carrier separation efficiency. However, as far as we know, there is no systematic study on Z-scheme R-TiO_2/A-TiO_2 photocatalysts, and the photocatalytic mechanism behind needs to be revealed.

Hence, in this study, we designed and prepared a ternary Z-type/Ⅱ-type scheme rutile TiO_2/ anatase TiO_2/ $ZrTiO_4$ (R-TiO_2/A-TiO_2/$ZrTiO_4$) photocatalyst via a facile one-step calcining strategy using H_3BO_3 as the dopant. A tunable rutile TiO_2/ anatase TiO_2 ratio (R/A) was achieved by changing the boron doping content. The photodegradation performance of Rhodamine B under visible light irradiation, and the stability of the obtained catalyst were evaluated. Besides, systematical characterization was employed to explore the composition, microstructure, optical properties and the photochemical properties of the materials. Especially, the utilization of visible light, the band structures, the generation, separation and transfer of the charge carriers in TiO_2 (A, R) /$ZrTiO_4$ was investigated to clarify the reason for the improved photocatalytic behaviour. This work provided an effective and simple

approach to design the bi-phase TiO_2 Z-scheme heterojunction, and the related photocatalytic mechanism was discussed.

2. Experimental section

2.1. Materials

Zirconyl chloride octahydrate ($ZrOCl_2 \cdot 8H_2O$, AR), Titanium sulfate ($Ti(SO_4)_2$, CP), Glucose ($C_6H_{12}O_6$, AR), Boric acid (H_3BO_3, AR), Hydrogen peroxide (H_2O_2, 35 wt%), Acetylacetone ($C_5H_8O_2$, AR), Ethanol (C_2H_6O, CP) and Rhodamine B (RhB, AR) were supplied by Sinopharm Chemical Reagent and used as received.

2.2. Preparation of Catalysts

The catalysts were prepared by a simple precursor preparation and calcination process. Firstly, solution A was obtained by adding (0.005 M) $ZrOCl_2 \cdot 8H_2O$ and (0.025 M) $Ti(SO_4)_2$ into 40 mL ethanol under constant stirring for 30 min, followed by adding 2 mL H_2O_2 and 5 mL $C_5H_8O_2$ with 1 h stirring to fully dissolve all the chemicals. Meanwhile, solution B was prepared by dissolving a certain amount of H_3BO_3 into 20 mL ethanol under constant stirring for 1 h. Similarly, solution C was made by dissolving (0.50 g) $C_6H_{12}O_6$ into 20 mL deionized water under constant stirring for 1 h. Secondly, solution B and solution C were added into solution A dropwise, respectively, followed by stirring for another 2 h to prepare the hybrid solution. Then the aimed precursor was obtained by fully drying the prepared hybrid solution at 60 ℃ for 48 h. Finally, the catalyst was synthesized by calcining the precursor at 800 ℃ for 2 h with a heating rate of 5 ℃/min in air. For the convenience of comparative analysis, H_3BO_3 of different dosages were used in the preparation of

solution B, based on a serial of B/Zr molar ratio, i.e., 0, 0.2, 0.4, 0.5, 0.55, 0.6, 0.7 and 0.75. Correspondingly, the obtained catalysts were labeled as 0-BZT, 20-BZT, 40-BZT, 50-BZT, 55-BZT, 60-BZT, 70-BZT, and 75-BZT, respectively.

2.3. Characterizations

The phases of the samples were measured by X-ray diffraction (XRD, D/max-2200PC, Rigaku, Japan, Cu Kα, λ = 0.15406 nm) in the 2θ range of 15~70° (40 kV, 40 mA). The component and molecular vibration of the samples were studied by a microscopic confocal laser Raman spectrometer (Raman, Renishaw-inVia, UK). The morphologies and the detailed structural features of the samples were studied by a scanning electron microscopy (SEM, FEI Verios 460, US), and a transmission electron microscope (TEM, FEI Tecnai G2 F20 S-TWIN, US) equipped with an energy-dispersive X-ray spectroscopy (EDS). Valence band (VB), composition and chemical state of the samples were analyzed by an X-ray photoelectron spectrometer (XPS, AXIS SUPRA, UK) with Al Kα X-ray source (10 mA, 15 kV) and C1s characteristic peak of 284.6 eV as the reference. UV-Vis diffuse reflectance spectra (UV-Vis DRS) of the samples were recorded on UV-Vis-NIR spectrophotometer (Cary 5000, US) at the wavelength of 200-800 nm, with an integrating sphere attachment and $BaSO_4$ reference. The photoluminescence (PL, excitation wavelength: 280 nm) spectra and time-resolved fluorescence (TR-PL, excitation wavelength: 340 nm) spectra were recorded on a fluorescence spectrophotometer (F-4600, Rigaku, Japan). The photocatalytic activities and the active species trapping experiments were measured by UV-Vis spectrophotometer (UV2800-A, UNICO, China). And the

electron spin resonance (EPR) spectra were obtained using a spectrometer (Bruker model A300, German) with a 300 W Xe lamp as the light source.

2.4. Photodegradation Procedure

The photocatalytic performances of the samples were determined through the degradation of RhB, using a 300 W Xe lamp as the visible light source. Typically, 30 mg photocatalyst was placed in 30 mL RhB solution (15 mg/L). Before illumination, the solution was kept in the dark for 10 min to achieve the adsorption equilibrium. Then the concentration of residue RhB during the reaction process was monitored by the UV-Vis spectrophotometer based on the characteristic absorption peak at the wavelength of 554 nm under illumination. The removal ratio (R) of the pollutant was calculated by equation (1):

$$R = (1 - C/C_0) \times 100\% \quad (1)$$

Where C_0 is the initial concentration of RhB, and C represents the concentration at given time intervals. Meanwhile, isopropyl alcohol (IPA), benzoquinone (BQ) and triethanolamine (TEOA) were applied as scavengers of hydroxyl radicals (•OH), superoxide radicals ($•O^{2-}$) and holes (h^+), respectively, during the scavenging experiments to determinate the active species during the RhB degradation. Besides, the powder after photodegradation reaction was collected after washing thoroughly and centrifugally separation by deionized water, and then the same procedure for photocatalytic degradation was run for another four times to check the recyclability of the photocatalyst.

2.5. Photoelectrochemical Measurement

The photoelectrochemical response was measured on an electrochemical workstation (CHI 760D, China) in a standard three-electrode system. During the test, a platinum wire was used as the counter electrode, Ag/AgCl was the reference electrode, and a fluorine-doped tin oxide glass (FTO, 2 cm ×2 cm) modified with the samples worked as the working electrode. The preparation method of the working electrode was described as follows: 5 mg of samples were dispersed into the mixed solution of 1 mL ethanol and 0.5 mL terpineol under ultrasonic treatment for 15 min. Then, 40 μL mixture was spread on a 2 cm ×2 cm FTO glass substrate, followed by 24 h drying in air. Moreover, all the transient photocurrent (TP) response, electrochemical impedance spectrum (EIS), and Mott–Schottky (M-S) plots were performed in 0.5 M Na_2SO_4 aqueous solution at a pH level of 7.1. Also, a 300 W Xe lamp was applied as the visible light source.

3. Results and discussion

3.1. Microstructural characterization of the photocatalysts

Figure 1 presents the XRD patterns and the Raman spectra of the samples with various amount of boron doping. In **Figure 1a**, sample 0-BZT only exhibits strong diffraction peaks at around 25.3°, 37.8°, 48.1°, 53.9° and 55.1°, ascribing to (101), (004), (200), (105) and (211) planes of anatase TiO_2 (A-TiO_2) (PDF 83-2243), respectively, and the other peaks at around 30.4° and 50.5° correspond to (111) and (022) planes of $ZrTiO_4$ (PDF 34-0415) [31,32]. From sample 20-BZT to 75-BZT, besides the existence of A-TiO_2 and $ZrTiO_4$ diffraction peaks, the peaks at around 27.4°, 36.1°, 54.3° and 56.6° correspond to (110), (101), (211) and (220) planes of

rutile TiO_2 (R-TiO_2) (PDF 76-1938), demonstrating the co-existence of A-TiO_2, $ZrTiO_4$ and R-TiO_2 in the composites. Moreover, the relative peak intensity of R-TiO_2/ A-TiO_2 was dramatically increased from 20-BZT to 75-BZT, suggesting that the major phase changed from A-TiO_2 into R-TiO_2 with the increasing of boron doping. Furthermore, **Table 1** presents the relative contents of each phases in all the samples determined from Rietveld method. As can be seen, the content of $ZrTiO_4$ in BZT was kept at around 25 wt%. The content of R-TiO_2 in BZT was increased from 0 to 74 wt% from 0-BZT to 75-BZT. The mass ratio of R-TiO_2/ A-TiO_2 increased from 0 (0-BZT) to 0.066 (50-BZT), and finally reached 61.67 (75-BZT), correspondingly.

Raman spectra of the samples were displayed in **Figure 1b**. For sample 0-BZT, the major bands at 142, 394, 515, and 639 cm^{-1} were observed, representing the typical characteristic Raman active modes ($3E_g$+B_{1g}+A_{1g}) of A-TiO_2 [33]. Similarly, with the increasing amount of boron doping, the gradually increased peak intensity of R-TiO_2 (236, 442, 623 cm^{-1}) Raman bands can be observed, verifying the increase of R-TiO_2 content [34].

Figure S1 shows the SEM images of as-prepared samples, from which an apparent morphology transformation can be observed. Specifically, the 0-BZT sample (**Figure 2a**) is composed of uniform and fine spherical particles in an average size of about 50 nm. The average particle size is significantly increased to nearly 100 nm for 50-BZT with a higher boron doping, as shown in **Figure 2b**. Moreover, the 75-BZT sample (**Figure 2c**) clearly consists of coarsened spherical, rhombic and ellipsoidal particles of different sizes ranging from about 100 nm to larger than 200 nm. TEM

and HRTEM were further applied to investigate the microstructure of as-prepared 50-BZT, and the result is shown in **Figure 3**. In **Figure 3a**, the composite has evenly distributed spherical, tetragon, and irregular nano-particles with the size around 20, 40, 70 nm, respectively, which are attributed to the co-existence of the A-TiO_2, R-TiO_2, and $ZrTiO_4$ phases. In **Figure 3b,** the lattice fringes of 0.351, 0.189, 0.169, 0.207, and 0.361 nm are ascribed to the (101), (200) crystal planes of A-TiO_2, (211) crystal plane of R-TiO_2, and (211), (011) crystal planes of $ZrTiO_4$, respectively [32,34,35]. It is noted that clear interface between A-TiO_2/R-TiO_2 and A-TiO_2/$ZrTiO_4$ can be observed, further confirming the successful development of heterointerface between the three phases, and the formation of R-TiO_2/A-TiO_2/$ZrTiO_4$ heterojunction, which is crucial for the separation of the photo-generated carriers in photocatalysis. The corresponding EDS mapping patterns of the selected area has been conducted and the results are shown in **Figure 3(c-h)**, indicating the homogeneous distribution of B, C, O, Ti and Zr elements throughout the detected region of 50-BZT. Furthermore, the EDS result indicates that boron atoms were successfully introduced into the composite.

To explore the detailed chemical state of the elements, XPS analysis was performed over all the samples, and the results are shown in **Figure S2**. In the XPS survey spectra of **Figure S2a and S2b**, all the BZT samples exhibit peaks related to the elements of B, C, O, Ti and Zr. From O_{1s} spectra in **Figure S2c and S2d**, all the samples mainly consist of five peaks, i.e. the peaks at around 529.2, 530.3, 531.5, 532.8, and 533.4 eV, which are assigned to lattice oxygen (L_O), Ti-O, vacancy oxygen (V_O), adsorbed oxygen (A_O) and O-H, respectively [36,37]. For the convenience of

analysis, the results of selected samples (0-BZT, 50-BZT and 75-BZT) were given in **Figure 4.** In **Figure 4a**, an observable blue shift can be observed for samples with the increasing amount of boron doping. It may be attributed to the increase of binding energy resulted from the increased boron atoms into the lattices of the A-TiO_2/R-TiO_2/$ZrTiO_4$ system [29]. As for the O_{1s} spectra in **Figure 4b,** compared with 0-BZT and 75-BZT, the component of vacancy oxygen for 50-BZT is much higher, indicating that the highest incorporation amount of boron into the crystal lattice might be achieved in this sample. Since the vacancy oxygen plays a major role in the band structure of semiconductor [38], the high component of vacancy oxygen in sample 50-BZT may be one reason for its better photo-degradation activity (as presented in section 3.2). **Figure 4c** shows Ti_{2p} spectra of the three samples. For sample 0-BZT, the spectrum can be divided into three peaks, and the peak at 458.0, 458.9 and 463.4 eV corresponds to the $Ti_{2p\ 3/2}$ in A-TiO_2, Ti-O-Zr bond, and $Ti_{2p\ 1/2}$ in A-TiO_2, respectively [39,40]. Compared with 0-BZT, a new peak at around 458.6 eV can be observed for 50-BZT, which is caused by the presence of R-TiO_2 [29,34]. Moreover, with increasing boron doping amount, the relative content of the peak at around 458.6 eV is increased, confirming the increasing content of R-TiO_2, which is in well agreement with the previous XRD and Raman results. In B_{1s} XPS spectra, the broad peaks can be divided into two peaks centered at around 197 eV and 195 eV, respectively. Considering the standard binding energy of B_{1s} in B_2O_3 or H_3BO_3 is around 194 eV [41], the appearance of the peak at around 195 eV indicates the possible formation of B_2O_3 microaggregates inside or on the surface of the

heterostructure [42,43]. Moreover, in sample 75-BZT, peaks ascribed to B_{1s} in B_2O_3 or H_3BO_3 appears with high intensity, implying that too high amount of boron loading did not contribute to a higher level of doping into the crystal structure, but caused the aggregates of B related species. Moreover, the peak at around 197 eV is not conclusively assigned and may be due to the chloride atoms (residue from zirconium source $ZrClO_4 \cdot 8H_2O$) bonded with boron atoms [44].

3.2. Photocatalytic activities of the photocatalysts

The photocatalytic activities of the constructed R-TiO_2/A-TiO_2/$ZrTiO_4$ heterojunctions were evaluated under visible-light using RhB as target pollutant. The results are shown in **Figure 5** and **Table 3**, while 0-BZT and P25 catalysts were used as references. The corresponding degradation curves are present in **Figure 5a**. RhB shows no self-degradation activity with visible light illumination, and all of the samples have no adsorption ability for RhB during the dark reaction. Compared with 0-BZT, an obvious positive effect on the photodegradation activity was observed, with the increasing amount of boron doping (from 20-BZT to 50-BZT). For sample 50-BZT, the degradation rate of RhB after visible light irradiation for 100 minutes was 97.8%, which was nearly 10 times higher than that of P25. Further increasing boron content from 55-BZT to 75-BZT, significant decrease in the degradation capacity was observed. According to the colour changes of the solutions after degradation reactions (inset pictures in **Fig 5a**), photodegradation performance of the samples can be easily verified. The kinetics of the degradation of RhB of all the samples is presented in **Fig 5b**. The RhB degradation rate of 50-BZT was 0.038 min^{-1},

which was 1.46 times higher than that of 0-BZT, and 38 times higher than the value of P25. Besides, the stability of 50-BZT was evaluated by conducting the RhB degradation experiment five times under the same condition, as shown in **Fig 5c**. The catalyst maintained the photodegradation efficiency with a less than 2% deduction after five cycles, indicating superior stability. Furthermore, the Raman spectra analysis of the fresh and tested 50-BZT in **Fig 5d** illustrate that the catalyst had stable structure after cycle experiments. These results demonstrate that the prepared BZT is a structure-stable and recyclable photocatalyst with high photocatalytic efficiency.

Combined with the result of XRD, the ability of RhB photodegradation of boron doped samples was improved gradually by increasing the mass ratio of R-TiO_2/A-TiO_2 from 0 to 0.066. And then, the photodegradation performance was deteriorated by further increasing the R-TiO_2 content. The result suggests that the low content of R-TiO_2 plays a crucial role in affecting the photo-degradation performance of BZT. In section 3.3, we will focus on clarifying the mechanism of the enhanced photocatalytic activity with the introduction of R-TiO_2.

3.3. Photocatalytic mechanism of the photocatalysts

Figure 6a shows the UV-Vis diffuse reflectance spectra (DRS) of the samples**.** All the samples have strong absorption in the UV and near-visible light. Compared with un-doped 0-BZT, samples with low mass ratio of R-TiO_2/A-TiO_2 (from 20-BZT to 50-BZT) presented an observable blue shift of the absorption edge. Further increasing the boron doping amount to 75-BZT, an apparent and continuous red shift of absorption edge was observed. The calculated bandgap Eg of the samples were

shown in **Fig 6b** and **Table 3**, according to equation (2) [45]:

$$\alpha h\nu = A\,(h\nu - Eg)^{n/2} \qquad (2)$$

where α is a constant, h denotes the Planck constant, ν represents frequency, A refers to the absorption coefficient near the absorption edge. The coefficient n is 4 in this work, because A-TiO_2, R-TiO_2 and $ZrTiO_4$ have indirect transition [46-48]. Similarly, bandgaps of the doped samples were narrowed from 2.84 eV (20-BZT) to 2.55 eV (75-BZT). Therefore, it can be concluded that visible light utilization can be enhanced with the increase of R-TiO_2/A-TiO_2 mass ratio in R-TiO_2/A-TiO_2/$ZrTiO_4$. Compared with A-TiO_2/$ZrTiO_4$ (0-BZT), low R-TiO_2/A-TiO_2 mass ratio (≤0.066) would have some negative effect on the efficiency of visible light utilization due to the slightly increase of the band-gap of the materials.

PL spectral studies were conducted, and the results were shown in **Fig 6c**. High PL intensity represents high rate of charge carrier recombination. Among all samples, sample 50-BZT shows the lowest PL intensity, suggesting the enhanced charge separation in optimized boron doped samples. Besides, much different curves were observed for the samples from 55-BZT to 75-BZT, due to the transformation of the major phase in the system. Additionally, the time-resolved transient PL decay (TR-PL) were measured to determine the recombination kinetics of photo-induced charge carriers and their average lifetimes, as shown in **Fig 6d**, which are fitted by a second-order exponential kinetics curve, based on equation (3) [49]:

$$\tau_{\mathrm{ave}} = (A_1\tau_1{}^2 + A_2\tau_2{}^2)/(A_1\tau_1 + A_2\tau_2) \qquad (3)$$

where A represents the amplitudes and τ denotes emission lifetimes of each

component. All the results of PL lifetime are presented in **Table 2**. Obviously, the lifetimes for 50-BZT (τ_1 = 0.12 ns, A_1 = 98.27%; τ_2 = 8.47 ns, A_2 = 1.73%) are much longer than those of 0-BZT (τ_1 = 0.11 ns, A_1 = 98.16%; τ_2 = 3.95 ns, A_2 = 1.84%). The prolonged lifetime indicates a longer duration time for photo-induced charger carriers kept at excited state, which may increase the probability of charge carriers participating in the following photodegradation reactions. However, 75-BZT with the longest lifetime did not perform a better photocatalytic activity, suggesting that the photoinduced carriers are easily excited but difficult to transfer, thus leading to the long PL lifetime but weak photocurrent, as verified by the following analysis.

From the transient photocurrent (TP) curves in **Fig 6e**, with a low R-TiO_2/A-TiO_2 mass ratio, the photocurrent intensity of the samples increased gradually from 0-BZT to 50-BZT. In **Fig 6f**, EIS plot of 50-BZT is the lowest among all the samples, indicating the charge carriers in the material possess the fastest separation and transfer rate. With a higher R-TiO_2/A-TiO_2 mass ratio from 55-BZT to 75-BZT, remarkably reduced photocurrent intensity was observed, which was also confirmed by the significantly increased EIS value in **Fig 6f.** These results are in good consistent with their photocatalytic behaviour. Therefore, it can be concluded that the R-TiO_2/A-TiO_2/$ZrTiO_4$ composites with appropriate component ratio possess significantly lowered recombination and high transportation of photogenerated electrons and holes, as a result of controlled B-doping content.

The band structures of all the samples were determined and shown in **Figure 7**. Considering a corrected value of a standard hydrogen electrode (0.63 eV, pH = 7) [50]

and the obtained XPS VB values in **Figure 7a and 7b**, the deduced valence band values of samples with low R-TiO_2/A-TiO_2 mass ratio (from 0-BZT to 50-BZT) increase from 2.07 to 2.21 eV. While this value decreased from 2.09 to 1.76 eV for samples with higher R-TiO_2 ratio (from 55-BZT to 75-BZT), as shown in **Figure 7d.** Based on the relation of $E_{CB} = E_{VB} - Eg$ [51], the conduction band values (E_{CB}) of the samples can be calculated to be from -0.67 to -0.79 eV, correspondingly. Moreover, Mott-Schottky analysis was conducted to obtain the electrochemical flat-band potentials (E_{fb}) of the samples. The Mott-Schottky plots with different frequencies (500, 1000, 1500 Hz) of the samples are shown in **Figure S3**, and the positive slope of the linear region demonstrates the n-type semiconductor [52]. Based on the potential relative to the Ag/AgCl reference electrode, the normal hydrogen electrode (NHE) potential was calculated according to equation (4) [53]:

$$E_{fb}\ (\text{vs. NHE}) = E_{fb}\ (\text{vs. Ag/AgCl}) + E_{AgCl} + 0.059 \times \text{pH} \qquad (4)$$

where E_{AgCl} is 0.197 V, and the pH is 7.10. E_{fb} (vs Ag/AgCl) and the calculated E_{fb} values of all samples are compared in **Figure 7c**. Considering E_{fb} of a n-type semiconductor is about 0.2 V below its CB potential [54], the CB positions of the samples can be deduced, which are in good consistent with the calculated CB value. In combination with the analysis above, schematic diagram of the band variations of the samples is given in **Figure 7d**. Obviously, boron doping is an effective approach to dominate the electronic band structure. Besides, the suitable band positions of the samples obtained from controlling the amount of boron dopant is crucial to enhance the redox ability and is helpful for the separation of photo-generated carriers.

Moreover, based on the results of E_{fb} values and the slopes of the Mott–Schottky plots, the charge carrier density (N_D) of the samples was calculated from equation (5) [54]:

$$N_D = \frac{2}{q\epsilon\epsilon_0}\frac{dE}{d\frac{1}{C^2}} = \frac{2}{q\epsilon\epsilon_0}\frac{1}{slope} \quad (5)$$

where q denotes the electronic charge (1.602×10^{-19} C), ε refers to the dielectric constant of TiO_2 (2.40), ε_0 is the permittivity (8.85×10^{-14} F·cm^{-2}) in vacuum, and the results are presented in **Table 3**. As can be seen, sample 50-BZT showed the highest carrier density, indicating the greater spatial separation of charge carriers.

To further clarify the generation of active species during the irradiation, the EPR measurement of sample 0-BZT, 50-BZT and 75-BZT was conducted, and the results are shown in **Figure S4**. During the test of vacancy, an apparent EPR signal at g = 2.001 was detected, suggesting the existence of the oxygen vacancy in the system [55]. Moreover, before and after illumination, the intensity of EPR signal ascribed to vacancy hardly changed (seen in **Figure S4a, S4d and S4g**), verifying the existence of oxygen vacancies, as revealed by the XPS analysis. Moreover, no signal was observed in the dark during the $\bullet O_2^-$ and •OH radicals trapping tests. In contrast, under visible light illumination, four strong signal peaks of DMPO-$\bullet O_2^-$ and DMPO-•OH with the intensity of 1:1:1:1 and 1:2:2:1 are detected over all the samples, indicating the generation of $\bullet O_2^-$ and •OH radicals during the photocatalytic reaction. The comparison result between these three samples is present in **Figure 8.** In the vacancy test of **Figure 8a**, compared with sample 0-BZT and 50-BZT, an extremely low signal was detected for sample 75-BZT, suggesting low content of oxygen

vacancy for high boron doped samples. In **Figure 8b**, the highest intensity of •OH radical was found for sample 50-BZT, resulted from its positive shift of the valence band position. In **Figure 8c**, decreased intensity of $•O_2^-$ radical with sample 50-BZT and 75-BZT could be observed, which might be attributed to the positive shift of the conduction band and the weakened transfer ability of charge carriers, respectively. Moreover, the EPR results are in good consistent with above analysis of band structures and the results of active species trapping experiments shown in **Figure S5.**

Based on the analysis above, a feasible photocatalytic mechanism of R-TiO_2/A-TiO_2/$ZrTiO_4$ is illustrated in **Figure 9**. Combined with energy band structure and band bending theory, a novel Z-scheme/Ⅱ-type R-TiO_2/A-TiO_2/$ZrTiO_4$ ternary heterojunction structure is obtained. Here, the band positions are reported on the basis of the energy values reported in ref 16, 56 and 57. Since R-TiO_2 has higher CB and VB positions and smaller work function (φ=4.2 eV) than A-TiO_2 (φ=8.1 eV) [58,59], when R-TiO_2 and A-TiO_2 are in contact, free electrons of R-TiO_2 can transfer to A-TiO_2 until their Fermi levels are equilibrated. Therefore, the R-TiO_2 side is positively charged, while A-TiO_2 side is negatively charged at the interface. Thus, an internal electric filed is formed and band edge bending occurs [60]. Furthermore, because R-TiO_2 has the smaller work function than A-TiO_2, i.e. a higher Fermi level, its band edge bends upward, hindering electrons transfer to A-TiO_2. And the build-in electric field as well as Coulomb repulsion also barricades possible electrons transfer from R-TiO_2 CB to A-TiO_2 CB. Similarly, these factors could also suppress the transfer of holes from VB of A-TiO_2 to VB of R-TiO_2. While, the existence of the

built-in electric field favors the recombination between the electrons in the CB of A-TiO_2 and the holes in the VB of R-TiO_2. This leads to direct Z-scheme electron transfer from the CB of A-TiO_2 to the VB of R-TiO_2. Importantly, the electrons from the CB of R-TiO_2 and the holes from the VB of A-TiO_2 are maintained and spatially separated. On the other hand, A-TiO_2 and $ZrTiO_4$ has similar band positions and staggered gaps, a typical Ⅱ-type charge transfer mode is preferred. The photo-induced electrons in the CB of $ZrTiO_4$ transfer to CB of A-TiO_2, and then recombine with the holes in the VB of R-TiO_2 with the existence of build-in electric field between the R-TiO_2 and A-TiO_2. Meanwhile, the holes in the VB of A-TiO_2 transfer to VB of $ZrTiO_4$. Moreover, the oxygen vacancies served as springboards to promote the separation and transfer of the photo-induced carriers. As a consequence, with stronger redox ability, the electrons accumulate in the CB of R-TiO_2, and the holes accumulate in the VB of $ZrTiO_4$. Subsequently, photo-induced electrons and holes react with O_2 and H_2O/OH^- to generate $\bullet O_2^-$ and •OH radicals, respectively, which will take part in the following photo-degradation of organic dyes.

4. Conclusions

Z-scheme/Ⅱ-type R-TiO_2/A-TiO_2/$ZrTiO_4$ ternary heterojunction photocatalysts were designed and successfully prepared using a simple one-step calcination strategy. The phase composition ratio of the R-TiO_2/A-TiO_2 and the band structure can be adjusted by controlling the amount of boron doping. With the increasing amount of boron doping, the content of $ZrTiO_4$ in BZT was kept at around 25 wt%. The content of R-TiO_2 in BZT was consistently increased from 0 to 74 wt% from 0-BZT to

75-BZT, while the material morphology evolved from uniform spherical particles into coarsened spherical, rhombic and ellipsoidal particles of different sizes. For as-prepared R-TiO_2/A-TiO_2/$ZrTiO_4$ photocatalysts, sample 50-BZT (R/A ratio, 0.066) had the lowest values of PL intensity and impedance, and the highest photocurrent intensity and density of charge carriers, making its superior photodegradation performance. Its RhB degradation rate was 97.8% after visible light irradiation for 100 minutes, about 10 times higher than P25. The excellent photodegradation performance was due to the remarkably enhanced separation and improved redox ability of the photo-induced charge carrier as a result of the formed rutile TiO_2/ anatase TiO_2 Z-scheme heterojunction and high content of oxygen vacancies.

Declaration of Competing Interest

The authors declare no competing financial interest.

Acknowledgments

This work was supported by the National Natural Science Foundation of China (grant numbers 51702194, 51302161); the Natural Science Foundation of Shaanxi Province (grant number 2018JQ5055, 2018GY-106); and the Research Startup Fund of Shaanxi University of Science and Technology (grant number 2016GBJ-09).

References

[1] L.F. Qi, Y.W. Yang, P.X. Zhang, Y. Le, C. Wang, T. Wu, Hierarchical flower-Like BiOIxBr(1-x) solid solution spheres with enhanced visible-light photocatalytic activity, Appl. Surf. Sci. 467-468 (2019) 792-801.

[2] H. Tong, S. Ouyang, Y. Bi, N. Umezawa, M. Oshikiri, J. Ye, Nano-photocatalytic materials: possibilities and challenges, Adv. Mater. 24 (2012) 229-251.

[3] T. Takata, K. Domen, Particulate Photocatalysts for Water splitting: recent advances and future prospects, ACS Energy Lett. 4 (2019) 542-549.

[4] M.N. Chong, B. Jin, C.W.K. Chow, C. Saint, Recent developments in photocatalytic water treatment technology: A review, Water. Res. 10 (2010) 2997-3027.

[5] A. Kudo, Y. Miseki, Heterogeneous photocatalyst materials for water splitting, Chem. Soc. Rev. 38 (2009) 253-278.

[6] S. Masudy-Panah, R.S. Moakhar, C.S. Chua, A. Khuswaha, G.K. Dalapati, Stable and efficient CuO based photocathode through oxygen-rich composition and Au-Pd nanostructure incorporation for solar-hydrogen production, ACS Appl. Mater. Inter. 9 (2017) 27596-27606.

[7] J. Ran, J. Zhang, J. Yu, M. Jaroniec, S.Z. Qiao, Earth abundant cocatalysts for semiconductor based photocatalytic water splitting, Chem. Soc. Rev. 43 (2014) 7787-7812.

[8] X. Wang, Z. Li, J. Shi, Y. Yu, One-dimensional titanium dioxide nanomaterials: Nanowires, nanorods, and nanobelts, Chem. Rev. 114 (2014) 9346-9384.

[9] K. Lee, A. Mazare, P. Schmuki, One-dimensional titanium dioxide nanomaterials: nanotubes, Chem. Rev. 114 (2014) 9385-9454.

[10] S.X. Liu, S.S. Yuan, Q.T. Zhang, B. Xu, C.Y. Wang, M. Zhang, T. Ohno, Fabrication and characterization of black TiO_2 with different Ti^{3+} concentrations

under atmospheric conditions, J. Catal. 366 (2018) 282-288.

[11] J.J. Yu, T.H. Wang, S. Rtimi, Magnetically separable TiO_2/FeOx/POM accelerating the photocatalytic removal of the emerging endocrine disruptor: 2,4-dichlorophenol, Appl. Catal. B-Environ. 254 (2019) 66-75.

[12] Q. Wei, W. Li, S.D. Wang, Y. Bai, Superior environment resistance of quartz crystal microbalance with anatase TiO_2/ZnO nanorod composite films, Appl. Surf. Sci. 347 (2015) 755-762.

[13] B.Z. Fang, Y.L. Xing, B. Arman, S.C. Zhang, D.P. Wilkinson, Hierarchical CuO–TiO_2 hollow microspheres for highly efficient photodriven reduction of CO_2 to CH_4, ACS Sustain. Chem. Eng. 3 (2015) 2381-2388.

[14] R. Sami, P. Cesar, S. Rosendo, N. Victor, L. Jean-Claude, K. John, Preparation and mechanism of Cu-decorated TiO_2–ZrO_2 films showing accelerated bacterial inactivation, ACS Appl. Mater. Inter. 7 (2015) 12832-12839.

[15] X.H. Feng, F.P. Pan, B.Z. Tran, Y. Li, Photocatalytic CO_2 reduction on porous TiO_2 synergistically promoted by atomic layer deposited MgO overcoating and photodeposited silver nanoparticles, Catal. Today 339 (2020) 328-336.

[16] C.Q. Liu, X. Li, Y.T. Wu, L. Sun, L.Y. Zhang, X.J. Chang, X.M. Zhang, X.F. Wang, Enhanced photocatalytic activity by tailoring the interface in TiO_2-$ZrTiO_4$ heterostructure in TiO_2-$ZrTiO_4$-SiO_2 ternary system, Ceram. Int. 45 (2019) 17163-17172.

[17] R.A. He, K.Y. Cheng, Z.Y. Wei, S.Y. Zhang, D.F. Xu, Room-temperature in situ fabrication and enhanced photocatalytic activity of direct Z-scheme BiOI/g-C_3N_4

photocatalyst, Appl. Surf. Sci. 465 (2019) 964-972.

[18] P. Zhou, J.G. Yu, M. Jaroniec, All-solid-state Z-scheme photocatalytic systems, Adv. Mater. 26 (2014) 4920-4935.

[19] J.X. Low, C.J. Jiang, B. Cheng, S. Wageh, A.A. Al-Ghamdi, J.G. Yu, A review of direct Z-scheme photocatalysts, Small Methods 1 (2017) 1700080.

[20] P. Wang, S. Zhan, Y. Xia, S. Ma, Q. Zhou, Y. Li, The fundamental role and mechanism of reduced graphene oxide in rGO/Pt-TiO_2 nanocomposite for high-performance photocatalytic water splitting, Appl. Catal., B-Environ. 207 (2017) 335-346.

[21] Q. G. Miguel, D. B. Nicolas, J. C. Claire, P. P. Ivan, Interstitial boron-doped TiO_2 thin films: The significant effect of boron on TiO_2 coatings grown by atmospheric pressure chemical vapor deposition, ACS Appl. Mater. Inter. 8 (2016) 25024-25029.

[22] B.F. Wang, F. Zhao, G.D. Du, S. Porter, Y. Liu, P. Zhang, Z.X. Cheng, H.K. Liu, Z.G. Huang, Boron-doped anatase TiO_2 as a high-performance anode material for sodium-ion batteries, ACS Appl. Mater. Inter. 8 (2016) 16009-16015.

[23] H.M. Hao, J.L. Shi, H. Xu, X. Li, X.J. Lang, N-hydroxyphthalimide-TiO_2 complex visible light photocatalysis, Appl. Catal. B-Environ. 246 (2019) 149-155.

[24] M. Pedrosa, L.M. Pastrana-Martínez, M.F.R. Pereira, J.L. Faria, A.M.T. Silva, N/S-doped graphene derivatives and TiO_2 for catalytic ozonation and photocatalysis of water pollutants, Chem. Eng. J. 348 (2018) 888-897.

[25] C.Y. Su, L.C. Wang, W.S. Liu, C.C. Wang, T.P. Perng, Photocatalysis and hydrogen evolution of Al- and Zn-doped TiO_2 nanotubes fabricated by atomic layer deposition, ACS Appl. Mater. Inter. 10 (2018) 33287-33295.

[26] J. Shao, W.C. Sheng, M.S. Wang, S.J. Li, J.R. Chen, Y. Zhang, S. Cao, In situ synthesis of carbon-doped TiO_2 single-crystal nanorods with a remarkably photocatalytic efficiency, Appl. Catal. B-Environ. 209 (2017) 311-319.

[27] N. Patel, A. Dashora, R. Jaiswal, R. Fernandes, M. Yadav, D.C. Kothari, B.L. Ahuja, A. Miotello, Experimental and theoretical investigations on the activity and stability of substitutional and interstitial boron in TiO_2 photocatalyst, J. Phys. Chem. C 119 (2015) 18581-18590.

[28] K. Wang, T. Peng, Z.M. Wang, H. Wang, X. Chen, W.X. Dai, X.Z. Fu, Correlation between the H_2 response and its oxidation over TiO_2 and N doped TiO_2 under UV irradiation induced by fermi level, Appl. Catal. B-Environ. 250 (2019) 89-98.

[29] W.K. Wang, J.J. Chen, M. Gao, Y.X. Huang, X. Zhang, H.Q. Yu, Photocatalytic degradation of atrazine by boron-doped TiO_2 with a tunable rutile/anatase ratio, Appl. Catal., B-Environ. 195 (2016) 69-76.

[30] F.Y. Xu, W. Xiao, B. Cheng, J.G. Yu, Direct Z-scheme anatase/rutile Bi-phase nanocomposite TiO_2 nanofiber photocatalyst with enhanced photocatalytic H_2-production activity, Int. J. Hydrogen Energ. 39 (2014) 15394-15402.

[31] Y.K. Kim, H.M. Jang, Polarization leakage and asymmetric raman line broadening in microwave dielectric $ZrTiO_4$, J. Phys. Chem. Solids 64 (2003)

1271-1278.

[32] A. George, S. Solomon, J.K. Thomas, A. John, Characterizations and electrical properties of $ZrTiO_4$ Ceramic, Mater. Res. Bull. 47 (2012) 3141-3147.

[33] S. Monica, I. Alina, D. Elena, B. Anca, D. Florian, T. Eugenia, C.N. Mihailescu, M. Ion, Direct nanocrystallite size investigation in microstrained mixed phase TiO_2 nanoparticles by PCA of raman spectra, Appl. Surf. Sci. 470 (2019) 507-519.

[34] X.C. Zhang, Y. Zhang, Z.K. Yu, X.R. Wei, W.D. Wu, X.N. Wang, Z.X. Wu, Facile synthesis of mesoporous anatase/rutile/hematite triple heterojunctions for superior heterogeneous photo-fenton catalysis, Appl. Catal. B-Environ. 263 (2020) 118335.

[35] T.C. Wei, Y.N. Zhu, X.Q. An, L.M. Liu, X.Z. Cao, H.J. Liu, J.H. Qu, Defect modulation of Z-Scheme TiO_2/Cu_2O photocatalysts for durable water splitting, ACS Catal. 9 (2019) 8346-8354.

[36] M. Wang, G.Q. Tan, H.J. Ren, A. Xia, Y. Liu, Direct double Z-scheme O-g-$C_3N_4/Zn_2SnO_4N/ZnO$ ternary heterojunction photocatalyst with enhanced visible photocatalytic activity, Appl. Surf. Sci. 492 (2019) 690-702.

[37] K. Wang, J. Li, G.K. Zhang, Ag-bridged Z- Scheme 2D/2D $Bi_5FeTi_3O_{15}$/g-C_3N_4 heterojunction for enhanced photocatalysis: Mediator-induced interfacial charge transfer and mechanism insights, ACS Appl. Mater. Inter. 11 (2019) 27686-27696.

[38] Y. Lu, X. Zhang, Y.C. Chu, H.B. Yu, X. Yuan, Cu_2O nanocrystals/TiO_2

microspheres film on a rotating disk containing long-afterglow phosphor for enhanced round-theclock photocatalysis, Appl. Catal. B-Environ. 224 (2018) 239-248.

[39] I. Hashemizadeh, V.B. Golovko, J. Choi, D.C.W. Tsang, A.C.K. Yip, Photocatalytic reduction of CO_2 to hydrocarbons using bio-templated porous TiO_2 architectures under UV and visible light, Chem. Eng. J. 347 (2018) 64-73.

[40] H.M. Hao, J.L. Shi, H. Xu, X. Li, X.J. Lang, N-hydroxyphthalimide-TiO_2 complex visible light photocatalysis, Appl. Catal. B-Environ. 246 (2019) 149-155.

[41] W. Zhao, W. Ma, C. Chem, J. Zhao, Z. Shuai, Efficient degradation of toxic organic pollutants with $Ni_2O_3/TiO_{2-x}B_x$ under visible irradiation, J. Am. Chem. Soc. 126 (2004) 4782-4783.

[42] G. Liu, X.X. Yan, Z.G. Chen, X.W. Wang, L.Z. Wang, G.Q. Lu, H.M. Cheng, Synthesis of rutile–anatase core–shell structured TiO_2 for photocatalysis, J. Mater. Chem. 19 (2009) 6590-6596.

[43] E. Finazzi, C.D. Valentin, G. Pacchioni, Boron-doped anatase TiO_2: Pure and hybrid DFT calculations, J. Phys. Chem. C 113 (2009) 220-228.

[44] G. Beshkov, D. Spassov, V. Krastev, P. Stefanov, S. Georgiev, S. Nemska, XPS study of BN_x nanolayers prepared by low pressure rapid thermal annealing in ammonia, J. Phys.: Conf. Ser. 113 (2008) 012046.

[45] X. Xu, X. Ding, X.L. Yang, P. Wang, S. Li, Z.X. Lu, H. Chen, Oxygen vacancy boosted photocatalytic decomposition of ciprofloxacin over Bi_2MoO_6: Oxygen

vacancy engineering, biotoxicity evaluation and mechanism study, J. Hazard. Mater. 364 (2019) 691-699.

[46] T. Baran, S. Wojtyła, A. Minguzzi, S.A. Rondinini, Achieving efficient H_2O_2 production by a visible-light absorbing, highly stable photosensitized TiO_2, Appl. Catal. B-Environ. 244 (2019) 303-312.

[47] Y. Zhao, C. Tao, G. Xiao, G. Wei, L. Li, C. Liu, H. Su, Controlled synthesis and photocatalysis of sea urchin-like Fe_3O_4@TiO_2@Ag nanocomposites, Nanoscale 8 (2016) 5313-5326.

[48] V.P. Aleria, A. Elisa, L. Stefano, I. Paulina, S. Zbigniew, P. Gianfranco, G. Elio, Fifty-fifty Zr-Ti solid solution with a TiO_2 type structure: electronic structure and photochemical properties of zirconium titanate $ZrTiO_4$, J. Phys. Chem. C 121 (2017) 5487-5497.

[49] Z.Y. Zhang, Y.Z. Huang, K.C. Liu, L.J. Guo, Q. Yuan, B. Dong, Multichannel improved charge-carrier dynamics in well-designed hetero-nanostructural plasmonic photocatalysts toward highly efficient solar-to-fuels conversion, Adv. Mater. 27 (2015) 5906-5914.

[50] B. Xia, Y. Yan, N. Li, H. Wu, X. Lou, X. Wang, A metal-organic framework-derived bifunctional oxygen electrocatalyst, Nat. Energy 1 (2016) 10566.

[51] P. Wang, B. Huang, X. Qin, X. Zhang, Y. Dai, J. Wei, M.H. Whangbo, Ag@AgCl: a highly efficient and stable photocatalyst active under visible light, Angew. Chem. Int. Ed. 47 (2008) 7931-7933.

[52] N. Bhandary, A.P. Singh, S. Kumar, P.P. Ingole, G.S. Thakur, A.K. Ganguli, S. Basu, In situ solid-state synthesis of a AgNi/g-C_3N_4 nanocomposite for enhanced photoelectrochemical and photocatalytic activity, ChemSusChem 9 (2016) 2816-2823.

[53] X.Q. An, K.F. Li, J.W. Tang, Cu_2O/reduced graphene oxide composites for the photocatalytic conversion of CO_2, ChemSusChem 7 (2014) 1086-1093.

[54] W.J. Yin, L.J. Bai, Y.Z. Zhu, S.X. Zhong, L.H. Zhao, Z.Q. Li, S. Bai, Embedding metal in the interface of a p-n heterojunction with a stack design for superior Z-scheme photocatalytic hydrogen evolution, ACS Appl. Mater. Inter. 8 (2016) 23133-23142.

[55] X. Xin, T. Xu, J. Yin, L. Wang, C. Wang, Management on the location and concentration of Ti^{3+} in anatase TiO_2 for defects-induced visible-light photocatalysis, Appl. Catal. B-Environ. 176-177 (2015) 354-362.

[56] Y.Q. Cao, T. He, Y.M. Chen and, Y.A. Cao, Fabrication of rutile TiO_2-Sn/anatase TiO_2-N heterostructure and its application in visible-light photocatalysis, J. Phys. Chem. C 114 (2010) 3627-3633.

[57] N.A. Deskins, R. Rousseau, M. Dupuis, Defining the role of excess electrons in the surface chemistry of TiO_2, J. Phys. Chem. C 114 (2010) 5891-5897.

[58] Y.H. Kim, S.Y. Lee, H.N. Umh, H.D. Song, J.W. Han, J.W. Choi, J. Yi, Directional change of interfacial electric field by carbon insertion in heterojunction system TiO_2/WO_3, ACS Appl. Mater. Interfaces 12 (2020) 15239-15245.

[59] A. Imanishi, E. Tsuji, Y. Nakato, Dependence of the work function of TiO_2 (rutile) on crystal faces, studied by a scanning auger microprobe, J. Phys. Chem. C 111 (2007) 2128-2132.

[60] Q.L. Xu, L.Y Zhang, J.G. Yu, S. Wageh, A.A. Al-Ghamdi, M. Jaroniec, Direct Z-scheme photocatalysts: principles, synthesis, and applications, Mater. Today 21 (2018) 1042-1063.

Table and Figure Captions:

Table 1 Phase compositions and mass ratios of R-TiO_2/A-TiO_2 in BZT samples

Table 2 Exponential decay-fitted parameters of fluorescence lifetime for BZT samples

Table 3 Photocatalytic degradation rates (R), kineties (k), band gap (Eg), and density of charge carriers (N_D) of BZT samples

Figure 1. (a) XRD patterns and (b) Raman spectra of the BZT samples

Figure 2. SEM images of (a) 0-BZT, (b) 50-BZT, and (c) 75-BZT samples

Figure 3. (a) TEM, (b) HRTEM, (c) HADDF images and EDS mappings of the B (d), C (e), O (f), Ti (g) and Zr (h) elements for 50-BZT

Figure 4. XPS spectra of 0, 50, 75-BZT: (a) survey, (b) O_{1s}, (c) Ti_{2p}, and (d) B_{1s}

Figure 5. (a) Photo-degradation curves of RhB over the BZT with various doping amount of boron, (b) Kinetics of the RhB degradation under visible light, (c) Cycled experiments of the 50-BZT, (d) Raman spectra of fresh and tested 50-BZT

Figure 6. (a) UV−Vis DRS, (b) Plot of $(\alpha h\nu)^2$ versus hν, (c) PL spectra, (d) TR-PL spectra, (e) TP curves, and (f) EIS plots of the BZT samples

Figure 7. (a, b) VB XPS spectra, (c) comparison of E_{fb} potential variations, and (d) schematic diagram of the band variations of the BZT samples

Figure 8. EPR spectra of (a) vacancy, (b) DMPO-•OH adducts in methanol solution, and (c) DMPO-•O_2^- adducts in aqueous solution recorded with 0, 50, 75-BZT under visible light irradiation

Figure 9. Photocatalytic mechanism of R-TiO_2/A-TiO_2/$ZrTiO_4$ under visible light illumination

Table 1 Phase compositions and mass ratios of R-TiO_2/A-TiO_2 in BZT samples

Samples	A-TiO_2/wt%	R-TiO_2/wt%	$ZrTiO_4$/ wt%	R-TiO_2/A-TiO_2 mass ratio
0-BZT	74.6	0	25.4	0
20-BZT	73.8	0.7	25.5	0009
40-BZT	72.5	1.7	25.8	0.023
50-BZT	69.2	4.6	26.2	0.066
55-BZT	42.4	31.5	26.1	0.743
60-BZT	13.5	60.7	25.8	4.796
70-BZT	2.3	72.1	25.6	31.35
75-BZT	1.2	74	24.8	61.67

Table 2 Exponential decay-fitted parameters of fluorescence lifetime for BZT samples

Samples	A_1	A_2	τ_1 (ns)	τ_2 (ns)	τ_{ave} (ns)
0-BZT	0.9816	0.0184	0.11	3.95	1.65
50-BZT	0.9827	0.0173	0.12	8.47	4.75
75-BZT	0.9821	0.0179	0.11	14.43	10.21

Table 3 Photocatalytic degradation rates (R), kineties (k), band gap (Eg), and density of charge carriers (N_D) of BZT samples

Samples	R (%)	k ($g \cdot min^{-1}$)	Eg (eV)	N_D (cm^{-3})
0-BZT	92.93	0.026	2.74	4.98×10^{22}
20-BZT	93.33	0.026	2.84	4.15×10^{22}
40-BZT	95.73	0.031	2.81	4.31×10^{22}
50-BZT	97.82	0.038	2.79	5.12×10^{22}
55-BZT	93.05	0.027	2.69	4.74×10^{22}
60-BZT	72.39	0.013	2.57	4.41×10^{22}
70-BZT	43.76	0.006	2.56	4.31×10^{22}
75-BZT	15.92	0.002	2.55	3.92×10^{22}

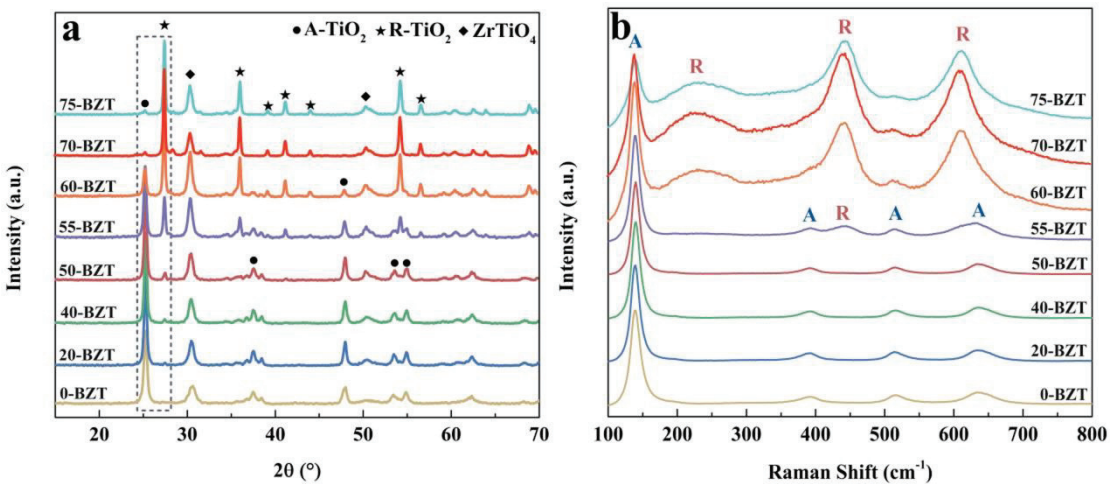

Figure 1. (a) XRD patterns and (b) Raman spectra of the BZT samples

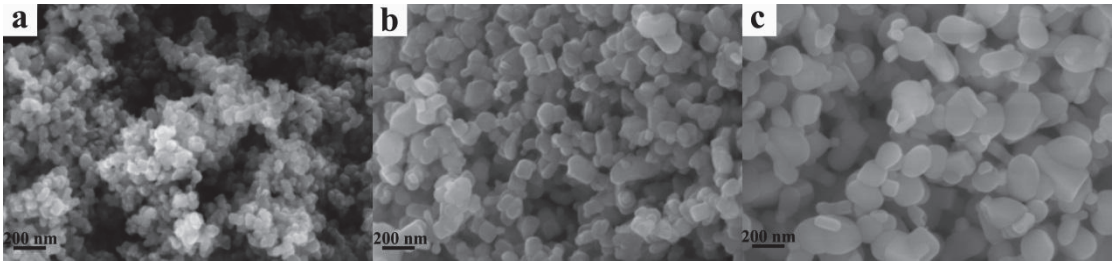

Figure 2. SEM images of (a) 0-BZT, (b) 50-BZT, and (c) 75-BZT samples

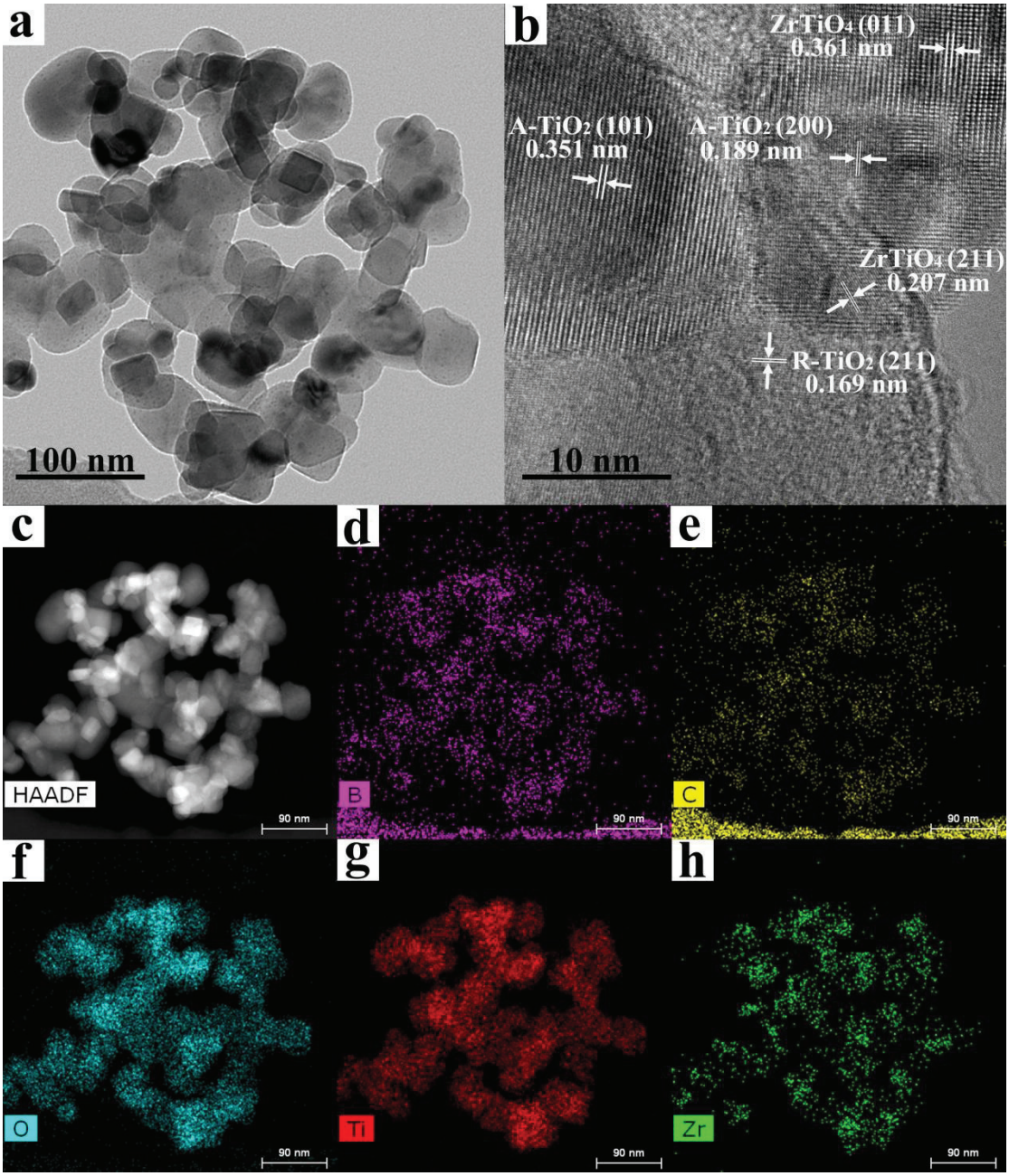

Figure 3. (a) TEM, (b) HRTEM, (c) HADDF images and EDS mappings of the B (d), C (e), O (f), Ti (g) and Zr (h) elements for 50-BZT

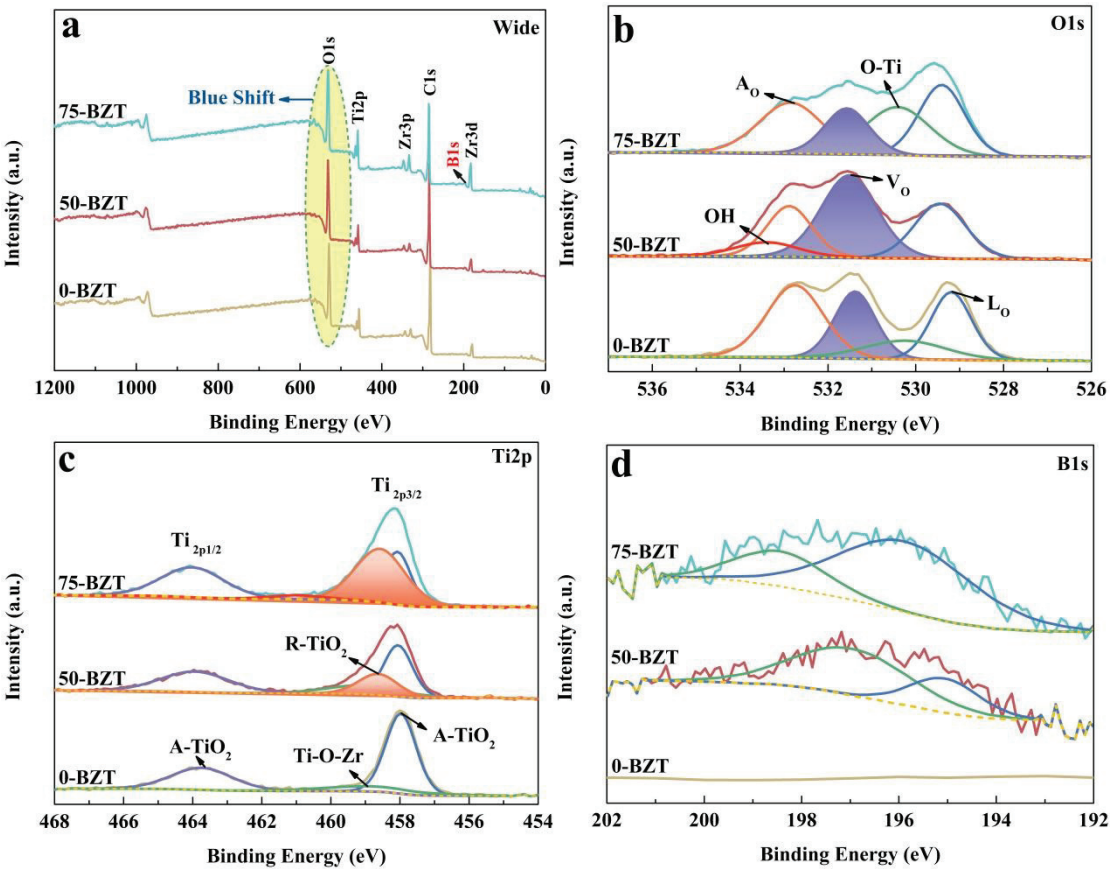

Figure 4. XPS spectra of 0, 50, 75-BZT: (a) survey, (b) O_{1s}, (c) Ti_{2p}, and (d) B_{1s}

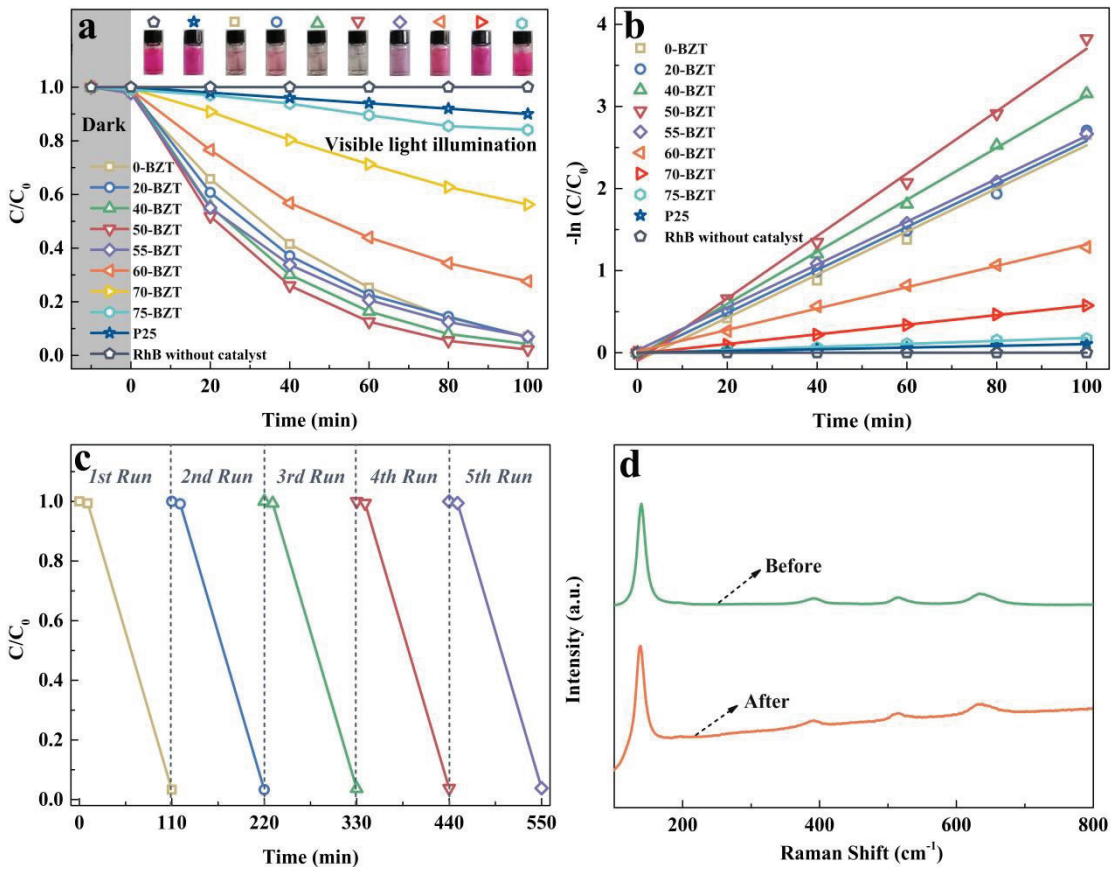

Figure 5. (a) Photo-degradation curves of RhB over the BZT with various doping amount of boron, (b) Kinetics of the RhB degradation under visible light, (c) Cycled experiments of the 50-BZT, (d) Raman spectra of fresh and tested 50-BZT

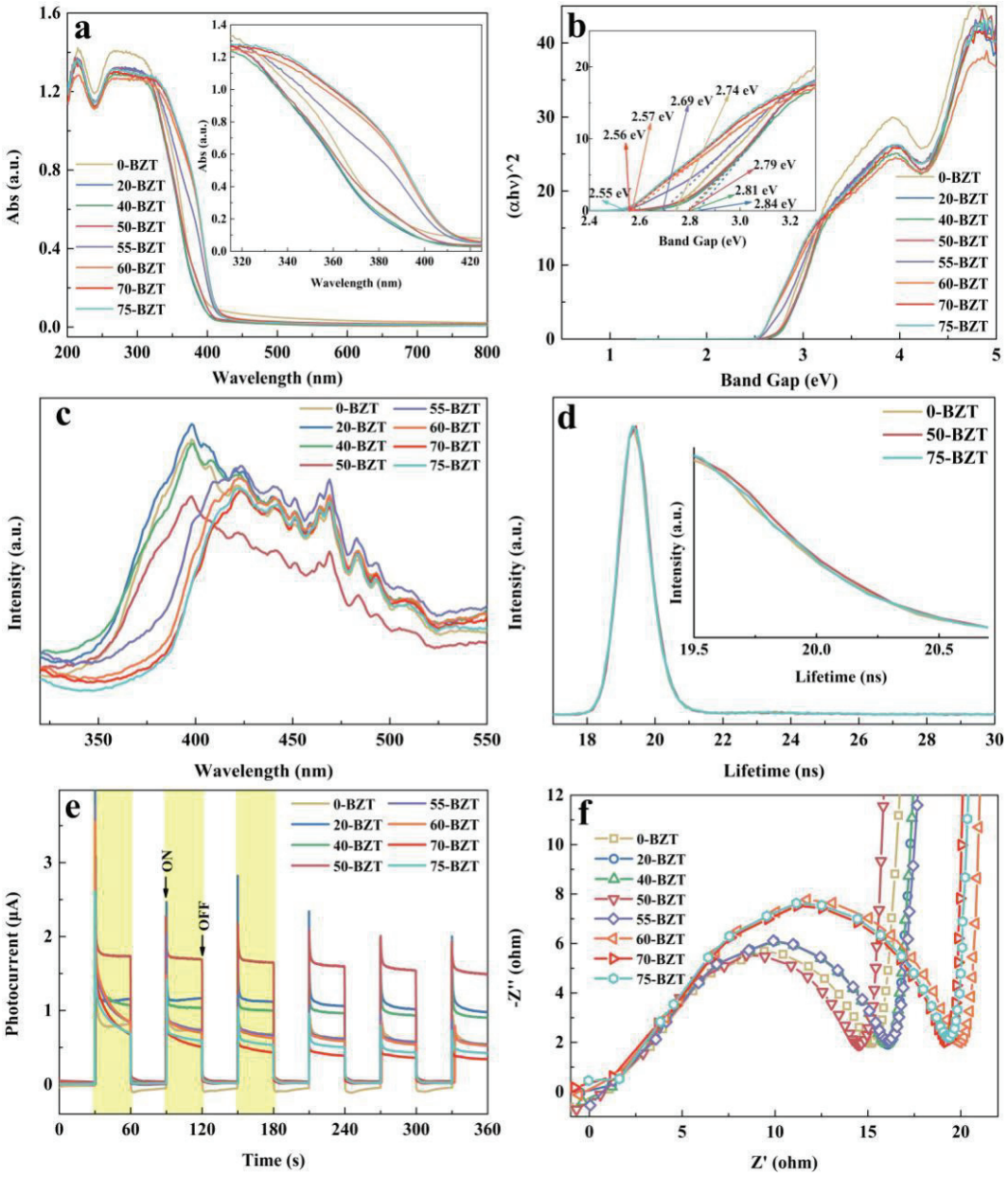

Figure 6. (a) UV−Vis DRS, (b) Plot of $(\alpha h\nu)^2$ versus hν, (c) PL spectra, (d) TR-PL spectra, (e) TP curves, and (f) EIS plots of the BZT samples

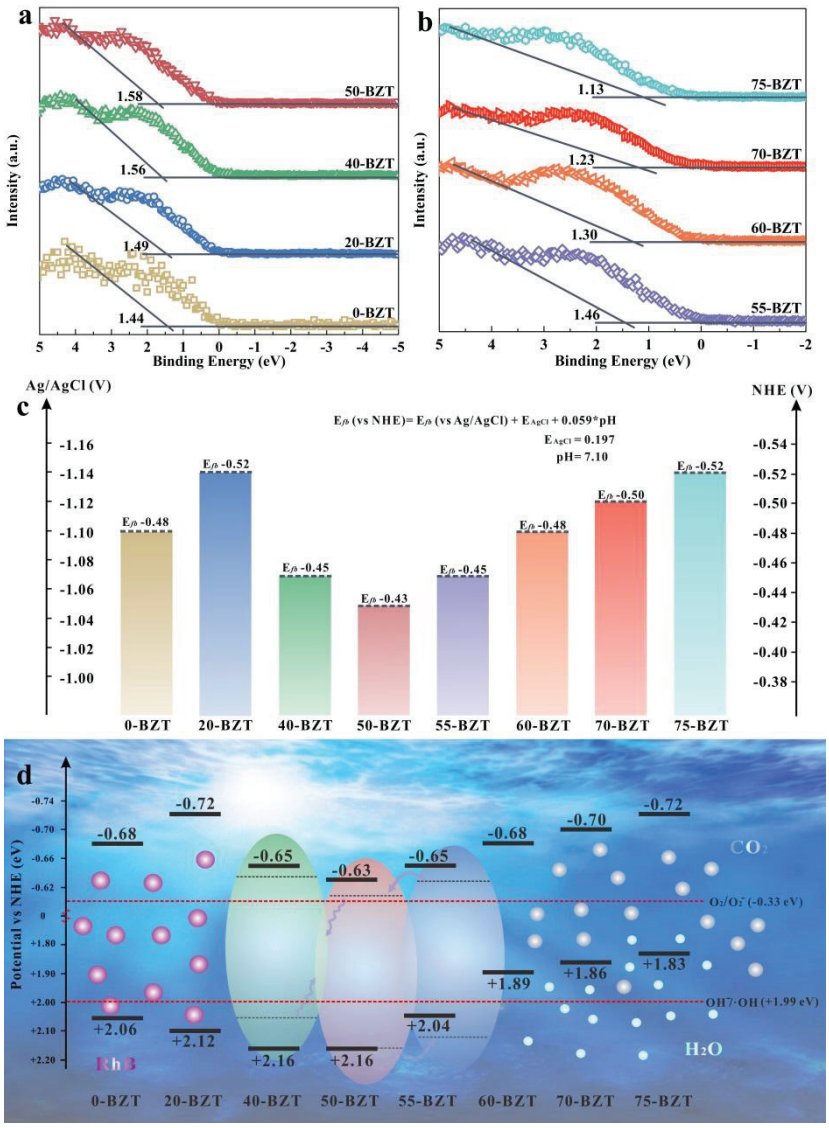

Figure 7. (a, b) VB XPS spectra, (c) comparison of E_{fb} potential variations, and (d) schematic diagram of the band variations of the BZT samples

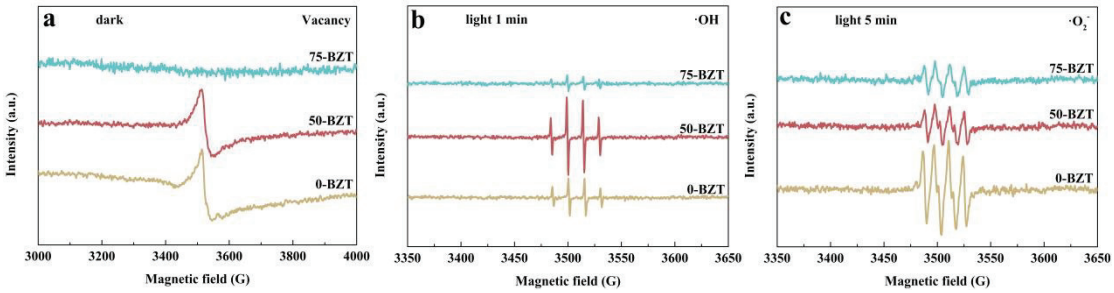

Figure 8. EPR spectra of (a) vacancy, (b) DMPO-•OH adducts in methanol solution, and (c) DMPO-•O_2^- adducts in aqueous solution recorded with 0, 50, 75-BZT under visible light irradiation

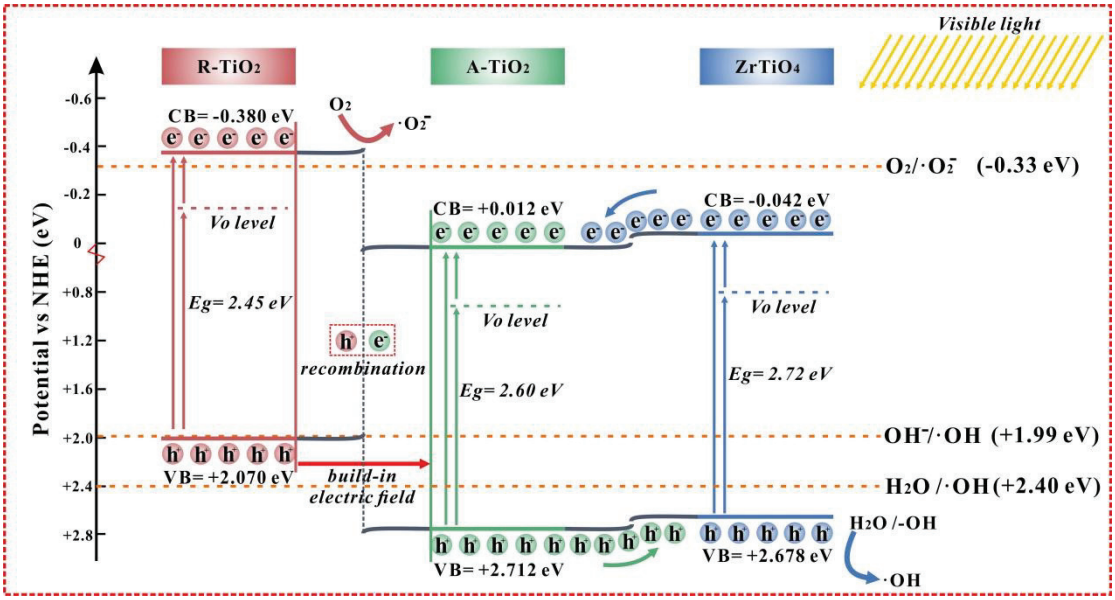

Figure 9. Photocatalytic mechanism of R-TiO_2/A-TiO_2/$ZrTiO_4$ under visible light illumination